Modeling of pneumatic melt drawing of polypropylene super-thin fibers in the Laval nozzle

A. BLIM, L. JARECKI*, and S. BLONSKI

Institute of Fundamental Technological Research of the Polish Academy of Sciences, 5B Pawinskiego St., 02-106 Warsaw, Poland

Abstract. Melt spinning of the fibers by supersonic air jet in the Laval nozzle is a novel, efficient and energy saving method of formation of super-thin fibers. In the process, polymer melt is extruded from a row of orifices and fast drawn by the pneumatic forces. In the modelling, air velocity, temperature and pressure distributions are computed from the k-ω aerodynamic model. Computations of the polymer air-drawing dynamics are based on the mathematical model of melt spinning in a single-, thin-filament approximation and Phan-Thien/Tanner non-linear viscoelasticity of the polymer melt. Axial profiles of the polymer velocity, temperature, tensile stress and rheological extra-pressure are computed. Influence of the Laval nozzle geometry, initial air compression, an initial melt temperature, a polymer mass output and the diameter of the melt extrusion die is discussed. The role of the polymer molecular weight, melt viscosity and relaxation time is considered. Example computations show the influence of important processing and material parameters. In the supersonic process, a high negative internal extra-pressure is predicted in the polymer melt under high elongation rates which may lead to cavitation and longitudinal burst splitting of the filament into a high number of sub-filaments. A hypothetical number of sub-filaments at the splitting is estimated from an energetic criterion. The diameter of the sub-filaments may reach the range of nano-fibers. A substantial influence of the Laval nozzle geometry is also predicted.

Key words: air-drawing, Laval nozzle, pneumatic melt spinning, superthin fibers.

1. Introduction

Pneumatic melt drawing with the use of the Laval nozzle is a novel and efficient method of formation of super-thin fibres. Super-fine fibres are characterized by a diameter in the range of 0.1–10 μm and a high ratio of polymer surface to its mass within the range of 0.5–40 m^2/g. The high surface expansion of those fibres is of great importance for environment protection, biotechnological and biomedical purposes. This new pneumatic technique is more efficient, at lower energy costs, and is much simpler in comparison with the *melt blown* method [1–3] which uses hot air streams blown from very narrow air slots. In the novel process, cold air is directed to the longitudinal Laval nozzle where the air stream, laminar at the entrance, and the polymer filaments strongly accelerate. As the air pressure at the nozzle inlet overcomes a critical value, the air jet achieves sound velocity in the narrowing of the nozzle and then accelerates to supersonic velocity in the nozzle divergent part.

In the processes with longitudinal spinning beams, the air jet streches aerodynamically the polymer streams directed to the nozzle from a single row of the spinneret orifices. A scheme of such longitudinal Laval nozzle-spinneret system used in the Nanoval process [4, 5] is shown in Fig. 1 in the cross-section normal to the spinning beam. The use of the Laval nozzle to form chemical fibres is an innovation which expands in a significant way the textile technology. The advantages of this method arise from the application of the spinneret orifices with larger diameter, in comparison with meltblowing which requires very fine spinneret orifices,

and 10–20 times higher mass throuhgput of the polymer per spinneret hole which results in much higher productivity of superthic fibers. The air slits can be wider by the order of magnitude. These make the process much easier to control, at the specific energy consumption for polymer heating and air-drawing by 3–5 times lower for obtaining filaments in the diameter range of 2–10 μm [4, 5]. The larger mass output allows to increase distances between the spinneret orifices and eliminate interconnections between the filaments occurring on the air-drawing axis.
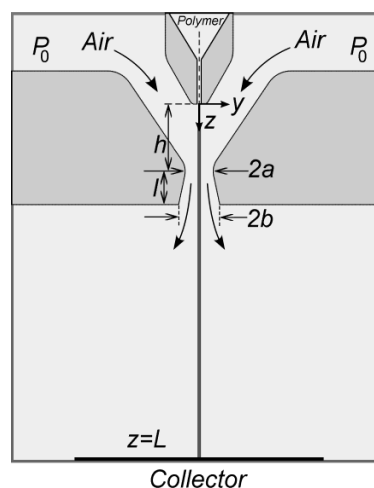

Fig. 1. Geometry of the die assembly with longitudinal Laval nozzle (normal cross-section) used in the modeling of the polymer melt air-drawing

*e-mail: ljarecki@ippt.pan.pl

Contrary to meltblowing, the process with the use of the Laval nozzle allows for obtaining continuous fibers without filaments molten together due to the use of cold air. The spinning equipment is simple and robust, and it also does not require application of special polymers of higher melt flow rates in order to save air heating energy. Throughput per unit of web can be double as high, while energy consumption is only about 20% that of meltblowing. What is more, the obtained fibres are continuous, thinner and stronger. This method can be applied for standard polymers like polypropylene, polyethylene, polyesters, polyamides, as well as for elastomers and polymers of biotechnological and biomedical use such as polylactides and cellulose. Future of the pneumatic method with the use of the Laval nozzle may be in applying it for natural polymers, aiming at reaching mechanical strength of super-thin fibers from the range of 0.5-5μm in the diamater produced for example by spiders.

2. Modeling of the air jet dynamics

In the literature, there is no work on modeling of the air jet dynamics in the Nanoval process of formation of super-thin fibers with the use of the longitudinal Laval nozzle. In this paper, the aerodynamic fields are determined for the geometry of the system shown in Fig. 1 in the cross-section normal to the longitudinal spinning beam with a single row of the spinneret orifices along the x-axis. The z-axis coincides with the axis of spinning. Experimental studies of the other authors [6–8] indicate that the impact of a single row of super-thin polymer streams (filaments) on the air jet dynamics can be omitted. Then, we apply distributions of the aerodynamic fields predetermined at the absence of the filaments as the air velocity, temperature and pressure fields at the pneumatic process. It is assumed in the literature in general that the air flow in the Laval nozzle should be laminar in spite of relatively high values of the Reynolds number [9, 10].

In the problem of air-drawing of the polymer filaments outside the Laval nozzle, we are interested in the dynamics of the air jet in the range between the nozzle outlet and the collector where the fibers are placed freely as a nonwoven. Due to strong interaction between the air blowing out of the nozzle with the air filling the outer space we should expect turbulent air flow in the domain of air-drawing of the filaments, as well as the dissipation effects. The presence of the ranges of laminar and probably turbulent nature in the air flow requires acting with a caution in the modeling of the air jet dynamics. On the one hand, it is important to avoid artificial turbulence in the area of laminar flow, but it is also important, on the other hand, not to suppress artificially fluctuations present in the turbulent area.

In the pneumatic melt spinning system with the Naval nozzle we deal with supersonic air velocities that generate high Reynolds numbers. Therefore, the air flow between the nozzle and the collector may have some features of a turbulent flow [11]. One of the most widely used models of the numerical flow mechanics is the k-ε model applied mainly for modeling of fully turbulent flows [12]. In the case of flows

that are not fully turbulent in the proximity of the Laval nozzle where a laminar-to-turbulent transition is expected, the k-ε model becomes insufficient. In such cases, the k-ω model is recommended [13–15].
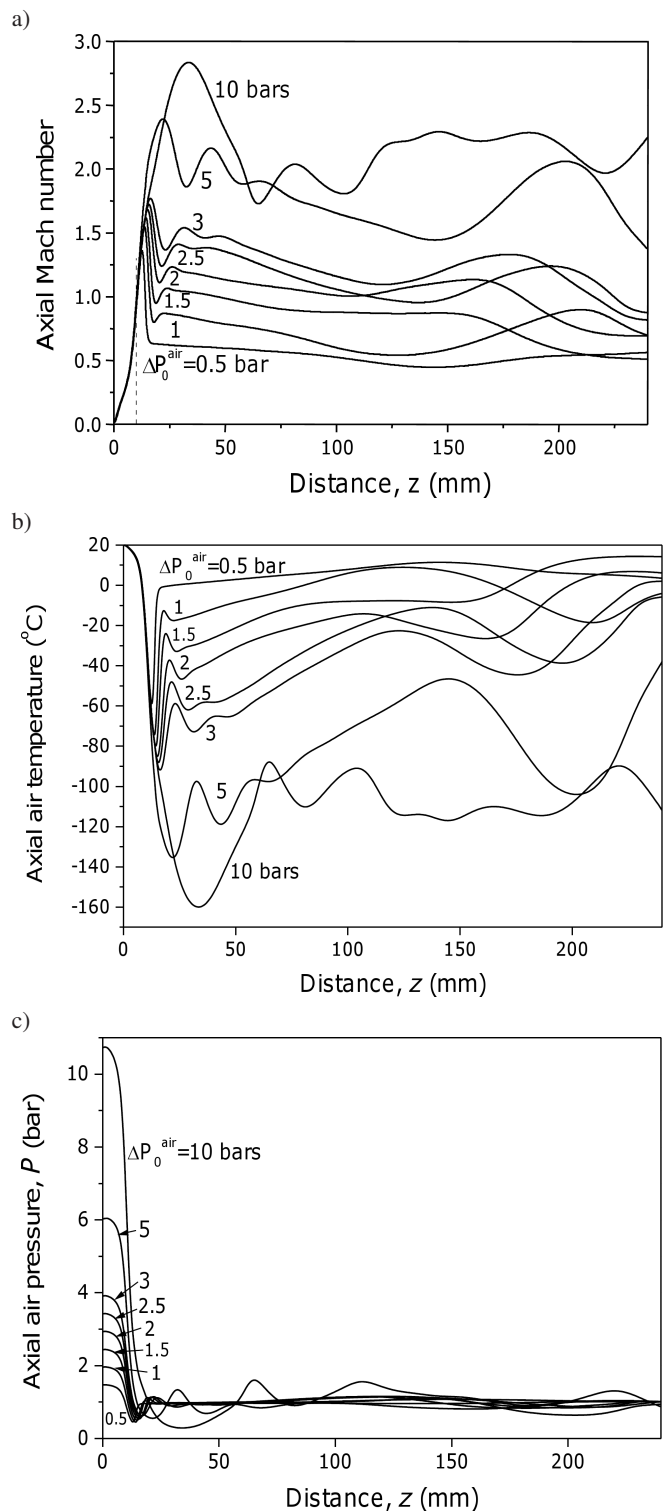

Fig. 2. Axial profiles of the Mach number (a), temperature (b), and air pressure (c) vs. distance z computed for the air compressions ΔP_0^{air} in the range 0.5–10 bars. Dotted line - position of the Laval nozzle narrowing

Simulations of the dynamic air fields are carried out using of the k-ω model of the fluid mechanics. In the model, $k = (\overline{u_i u_i})/2$ is the average turbulent kinetic energy, $\omega = \varepsilon/k$ – the specific dissipation rate where $\varepsilon = \nu \cdot \left(\dfrac{\partial u_i}{\partial x_j} \cdot \dfrac{\partial u_j}{\partial x_i}\right)$, ν – kinematic viscosity of the air. Compressible, steady-state two-dimensional air flow is considered in the (y, z) plane where the coordinate system with the z-axis identical with the symmetry axis of the normal cross-section of the die assembly and the spinning axis is considered (Fig. 1). The computational domain is limited to the half-plane determined by the symmetry z-axis. The computations have been performed with the aid of the Fluent package with the use of finite volume elements method of CFD. In the modeling, the Mach number, temperature and air pressure distributions along the symmetry z-axis of the jet ($y = 0$) are obtained between the spinneret orifice ($z = 0$) and domain limit ($z = 240$ mm), presented in Fig. 2(a-c) for different air compression ΔP_0^{air} in the Laval nozzle inlet in the range of 0.5–10 bars (1 bar = 10^5 Pa).

3. Modeling of uniaxial air-drawing of the polymer melt

The mathematical model of pneumatic melt spinning consists of a set of the balance equations for the mass, momentum and heat energy of the air-drawn filament, the constitutive equations and the equations of the polymer structure formation in thin-filament approximation. The air jet conditions around the filament are pre-determined by the velocity, temperature and air pressure distributions along the z-axis basing on the numerical criteria of the k-ω model of stationary air jet.

The equation of mass balance of the filament on the spinning axis determines the dependence between the local filament velocity $V(z)$ and its diameter $D(z)$ [16]

$$\frac{\pi D^2(z)}{4}\rho(z)V(z) = W, \tag{1}$$

where W – polymer mass output per single spinneret hole, $\rho(z) = \rho_0/\left[1 + \rho_1[T(z) - 273]\right]$ – polymer density dependent on local temperature $T(z)$, and ρ_0, ρ_1 are constants.

Change of the rheological force $F(z)$ on a differential portion dz of the filament fulfils the following differential equation of the force balance [16, 17]

$$\frac{dF}{dz} = W\frac{dV}{dz} - \frac{\pi D^2(z)}{4}\rho(z)g + \pi D(z)p_{zr}(z), \tag{2}$$

where

$$p_{zr}(z) = \frac{1}{2}\rho_a(z)C_f(z)\left[V(z) - U_z(z)\right]^2 \text{sign}\left[V(z) - U_z(z)\right]$$

is local shear stress of the air friction forces on the filament surface along the z-axis, tangential to the filament surface and resulting from the difference in the local axial velocity of the air, $U_z(z)$, and the polymer, $V(z)$. $\rho_a(z)$ is the air density dependent on local temperature and pressure, g – gravity. The air friction coefficient

$$C_f(z) = \beta Re_D^{-\alpha}(z) = \beta\left[\frac{D(z)\,|V(z) - U_z(z)|}{\nu_a(z)}\right]^{-\alpha}$$

where $\nu_a(z)$ is kinematic air viscosity, α and β are constants. In the case of pneumatic melt spinning we have $\alpha = 0.61$, $\beta = 0.78$ [18, 19].

Axial distribution of the air jet velocity in the range $z \in [0,\ z*]$ is approximated by the continuous function

$$U_z(z) = A_0 + A \cdot u(z)$$

where

$$u(z) = 1/\left[1 + \sum_{i=1}^{3} A_i\left[2\left(z - z_a\right)/w\right]^{2i}\right],$$

and in the range

$$z \in [z*,\ L]$$

by the function

$$U_z(z) = B_0 + \sum_{i=1}^{5} B_i z^i,$$

obtained from the approximation of the computer simulation data with the use of the Origin 6.0 software.

When the air velocity exceeds local velocity of the filament, $U_z(z) > V(z)$, the local shear stress p_{zr} is negative. Then, the negative axial gradient of the aerodynamic force leads to accumulation of the tensile force in the filament at the initial part of the process axis. The accumulation of the tension results in a strong decrease of the filament diameter observed near the Laval nozzle on a very short segment of 1–2 cm in the length.

The density $\rho_a(z) = \text{const}\ P_a(z)/T_a(z)$ and kinematic viscosity of dry air

$$\nu_a(z) = \frac{\eta_a(z)}{\rho_a(z)} = \text{const}\frac{T_{ref}+114}{T_a(z)+114}\left[\frac{T_a(z)}{T_{ref}}\right]^{3/2}\frac{T_a(z)}{P_a(z)}\eta_a(T_{ref})$$

depend on local air temperature $T_a(z)$ and pressure $P_a(z)$ on the air-polymer boundary. $\eta_a(z)$ and $\eta_a(T_{ref})$ are the dynamic air viscosities, local at the point z and at a reference temperature T_{ref}. For dry air under atmospheric pressure we have $\rho_a(z) = 0.35232/T_a(z)$ (g/cm^3) and $\nu_a(z) = 4.1618 \times 10^{-5}T_a^{5/2}(z)/\left[T_a(z) + 114\right]$ (cm^2/s).

The heat balance equation for the differential portion dz of the polymer filament

$$\rho(z)C_p(z)V(z)\frac{dT}{dz} = -\frac{4\alpha*(z)}{D(z)}\left[T(z) - T_a(z)\right]$$

$$+\rho(z)\Delta h\dot{X}(z) + tr\left[\boldsymbol{\sigma}(z) \cdot \dot{\mathbf{e}}(z)\right] \tag{3}$$

determines axial gradient dT/dz of the filament temperature controlled by the convective heat exchange coefficient $\alpha*$ between the filament moving with axial velocity $V(z)$ and the air jet of local velocity $U_z(z)$, the heat of polymer crystallization proportional to the local crystallization rate $\dot{X}(z)$, and by the heat of viscous friction generated in the polymer bulk under local stress during fast drawing [16, 17]. $C_p(z) = C_{p0} + C_{p1}\left[T(z) - 273\right]$ is the polymer specific heat dependent on local temperature, C_{p0}, C_{p1} – constants, Δh – heat of crystallization per unit polymer mass, $\boldsymbol{\sigma}(z)$, $\dot{\mathbf{e}}(z)$ – local stress and deformation rate tensors of uniaxial drawing of the polymer.

The convective heat exchange coefficient $\alpha*$ is determined from the experimental correlation between the Nusselt and Reynolds numbers [20, 21] $\alpha*D(z)/\lambda_a(z) = 0.42\,\mathrm{Re}_D^{0.334}(z)$ where $\lambda_a(z) = \dfrac{T_{ref}+114}{T_a(z)+114}\left(\dfrac{T_a(z)}{T_{ref}}\right)^{3/2}\lambda_0(T_{ref})$ is the air heat conductivity coefficient and λ_0 – the coefficient at a reference temperature T_{ref}. In the case of the air under atmospheric pressure $\lambda_a(z) = 2.0852 \times 10^{-5}T_a^{3/2}(z)/\left[T_a(z)+114\right]$ (J/(cm·s· K)). Based on the experimental correlation with the transverse air velocity component being zero we have

$$\alpha*(z) = 1.7585\frac{\lambda_a(z)}{\nu_a^{0.334}(z)}$$
$$\cdot\frac{|V(z)-U_z(z)|^{0.334}}{D^{0.666}(z)}\quad\text{(J/(cm}^2\cdot\text{s}\cdot\text{K))}, \tag{4}$$

where the diameter $D(z)$ expresses in cm, and V, U_z in cm/s.

The stresses in the polymer are determined from the rheological constitutive equation. Uniaxial stretching of the polymer melt leads to uniaxial extra-stress tensor with the axial, σ_{zz}, and radial, σ_{rr}, components. The components expressed by the tensile stress $\Delta p = \sigma_{zz}-\sigma_{rr}$ and the extra rheological pressure $p_{rh} = -\left(\sigma_{zz}+2\sigma_{rr}\right)/3$ read $\sigma_{zz} = \frac{2}{3}\Delta p - p_{rh}$ and $\sigma_{rr} = -\frac{1}{3}\Delta p - p_{rh}$. Local tensile stress of the filament results from the local rheological force $F(z)$ and reads $\Delta p(z) = \dfrac{F(z)}{\pi D^2(z)}$.

Due to high filament elongation rates, Phan-Thien/Tanner constitutive equation of non-linear viscoelasticity is used that apart from the local shear viscosity $\eta(z)$ and the relaxation time $\tau(z)$ introduces material parameters ε and ξ responsible for non-linear elasticity and shear thinning effects [22]. For uniaxial tension, the constitutive equation in thin-filament approximation leads to the set of two equations involving axial velocity gradient dV/dz, local tensile stress $\Delta p(z)$ and rheological extra-pressure $p_{rh}(z)$ [23]

$$\tau(z)V(z)\frac{d}{dz}\Delta p + \Delta p(z)\,\exp\left[-3\varepsilon\frac{\tau(z)}{\eta(z)}p_{rh}(z)\right]$$
$$= 3\eta(z)\frac{dV}{dz} + \tau(z)(1-\xi)\left[\Delta p - 3p_{rh}(z)\right]\frac{dV}{dz}. \tag{5}$$

$$\tau(z)V(z)\frac{d}{dz}p_{rh} + p_{rh}(z)\exp\left[-3\varepsilon\frac{\tau(z)}{\eta(z)}p_{rh}(z)\right]$$
$$= -\frac{2}{3}\tau(z)(1-\xi)\Delta p(z)\frac{dV}{dz}. \tag{6}$$

For isotactic polypropylene (iPP) we assume $\varepsilon = 0.015$, $\xi = 0.6$ [23].

Polymer viscosity $\eta(z)$ and the relaxation time $\tau(z)$ strongly depend on the local temperature $T(z)$, the average molecular weight M_w, and the local degree of crystallinity $X(z)$ [24]. Crystallization leads to a jelly-like structure of the polymer with crystalline aggregates acting as physical cross-links and thus to an increase of local viscosity and the

relaxation time until solidification of the material at a critical degree of crystallinity $X*$. These material functions are expressed by the product of the melt viscosity, or the melt relaxation time, and the functions responsible for the effects of crystallinity [16, 25]

$$\eta(z) = \eta_{melt}\left[M_w, T(z)\right]\cdot\frac{1}{1-X(z)/X*}, \tag{7a}$$

$$\tau(z) = \tau_{melt}\left[M_w, T(z)\right]\cdot\frac{\exp\left[3.2X(z)/X_\infty\right]}{1-X(z)/X*}, \tag{7b}$$

where $X*$ – the critical degree of crystallinity at the polymer solidification, X_∞ – maximum degree of crystallinity achievable by the polymer. For iPP we assume $X* = 0.1$ and $X_\infty = 0.55$ [25, 26] in the modelling.

The temperature dependence of the melt shear viscosity

$$\eta_{melt}\left[M_w, T(z)\right] = \begin{cases} \eta_0 M_w^\mu \exp\left[E_D/kT(z)\right] & T > T_g \\ \infty & T \le T_g \end{cases}, \tag{8}$$

where E_D is the activation energy, T_g – glass transition temperature. In the case of iPP we have $\mu = 3.4$ [27] and $E_D/k = 5292$ [28]. The constant $\eta_0 = \eta_{melt}^{ref}/\left[\left(M_w^{ref}\right)^\mu \exp\left(E_D/kT_{ref}\right)\right]$ is expressed by the reference shear viscosity η_{melt}^{ref} of the melt with the polymer average molecular weight M_w^{ref} at a reference temperature T_{ref}. The reference melt viscosity $\eta_{melt}^{ref} = 3000$ Pa·s at 220°C and the average molecular weight $M_w^{ref} = 300,000$ are chosen for iPP [27].

The local relaxation time of the melt is determined from the ratio of shear viscosity $\eta_{melt}(z)$ and the modulus of elasticity $G_{melt}(z)$

$$\tau_{melt}\left[M_w, T(z)\right] = \frac{\eta_{melt}(z)}{G_{melt}(z)}$$
$$= \begin{cases} \tau_0[M_w^\mu/T(z)]\exp\left[E_D/kT(z)\right] & T > T_g \\ \infty & T \le T_g \end{cases}, \tag{9}$$

where $\tau_0 = \tau_{melt}^{ref}T_{ref}/\left[\left(M_w^{ref}\right)^\mu \exp\left(E_D/kT_{ref}\right)\right]$ expresses by the reference relaxation time τ_{melt}^{ref} of the polymer melt with the reference molecular weight M_w^{ref} at the reference temperature T_{ref}. For iPP we have $\tau_{melt}^{ref} = 0.035$s at $T_{ref} = 220$°C and $M_w^{ref} = 300,000$ [23, 25].

Under the tensile stress, uniaxial molecular orientation of the polymer melt is formed in the filament at the air-drawing. Fast drawing of the filament is observed in the pneumatic melt spinning under supersonic air jets, located in relatively narrow range of the spinning axis next to the extrusion point. And so, non-linear stress-optical relation is used to specify local birefringence of the amorphous polymer, $\Delta n_a(z)$, and local amorphous orientation factor, $f_a(z)$, under the tensile stress $\Delta p(z)$, derived basing on the non-Gaussian conformational statistics of flexible chain macromolecules [29]:

$$f_a(z) = \frac{\Delta n_a(z)}{\Delta n_a^0} = \frac{C_{opt}}{\Delta n_a^0}$$
$$\cdot\left[1 - \frac{3}{7}\frac{C_{opt}}{\Delta n_a^0}\Delta p(z) - \frac{1}{7}\left(\frac{C_{opt}}{\Delta n_a^0}\right)^2\Delta p^2(z)\right]\Delta p(z), \tag{10}$$

where Δn_a^0 – amorphous birefringence of ideally oriented chains, C_{opt} – the stress-optical coefficient. For iPP we assume $\Delta n_a^0 = 0.060$ and $C_{opt} = 9.0 \times 10^{-10}$ m^2/N [30].

Molecular orientation during the pneumatic process may lead to on-line oriented crystallization under variable temperature on the processing axis z and to significant increase of the polymer viscosity and tensile stresses due to the crystallization. Local crystallization rate is determined from the differential form of the Avrami equation [31, 32]

$$\dot{X}(z) = V(z)\frac{dX}{dz} = n(1-X)\left[-\ln(1-X)\right]^{1-1/n} K(z)$$
(11)

with the local crystallization rate function

$$K(z) = K[T(z), f_a(z)]$$
$$= K_{\max} \exp\left[-4\ln(2)\frac{(T-T_{\max})^2}{D_{1/2}^2}\right] \exp\left(Af_a^2\right)$$
(12)

as dependent on the local melt temperature $T(z)$ and the local Hermans amorphous orientation factor $f_a(z)$. $K_{\max}$, $T_{\max}$, $D_{1/2}$ and $A > 0$ are material parameters. The Avrami index $n = 2$ is assumed for the on-line oriented crystallization [29].

Equation (12) has been proposed by Ziabicki [16] for non-isothermal, oriented crystallization in quasistatic approximation and not too high amorphous orientations basing on phenomenological analysis and symmetry reasons where the parameter A can be determined from an independent experiment [33]. An overview of the approaches to include non-isothermal and oriented crystallization effects in the modelling of fiber melt spinning has been given by Spruiell [34]. Following Katayama and Yoon [35], Spruiell and coworkers [36, 37] proposed the following crystallization rate function

$$K(z) = K[T(z), f_a(z)] = K_0 \exp\left[-\frac{U^*}{k(T-T_\infty)}\right]$$
$$\cdot \exp\left[-\frac{C_3}{T\Delta T + CT^2 f_a^2}\right]$$
(13)

derived basing on the crystal nucleation and growth rate theory under uniaxial extension of the chain macromolecules in the melt in the linear rubber elasticity approach. U^* is the activation energy for segmental jumping, $T_\infty = T_g - 30$, $\Delta T = T_m^0 - T$, and K_0, C, C_3 are experimental constants.

Transient and athermal effects in the crystallization kinetics associated with fast temperature and stress changes are neglected. The crystallization rate functions for oriented crystallization, Eqs. (12), (13), base on average amorphous orientation value and they neglect "selective" oriented crystallization and its role in the orientation distribution of amorphous segments development [38].

With the assumption of small amorphous orientation factor f_a, the crystallization rate function derived from the nucleation and growth rate theory, Eq. (13), can be presented in the form with separated amorphous orientation contribution. The orientation-dependent exponent in Eq. (13) presented in the form of the series expansion over f_a and accountig for the first orientation term reads $-\frac{C_3}{T\Delta T + CT^2 f_a^2} \cong -\frac{C_3}{T\Delta T} + \frac{C_3 C}{(\Delta T)^2} f_a^2$. Considering the expansion, from comparison of Eqs. (12) and (13), the phenomenological oriented crystallization coefficient $A = \frac{C_3 C}{(\Delta T)^2}$ expresses in terms of the values used in the nucleation and growth theory, while the thermal contribution to the crystallization kinetics is approximated by the Gaussian relation, $K_0 \exp\left[-\frac{U^*}{k(T-T_\infty)}\right] \exp\left(-\frac{C_3}{T\Delta T}\right) \cong K_{\max} \exp\left[-4\ln(2)\frac{(T-T_{\max})^2}{D_{1/2}^2}\right]$. However, the crystallizatition rate function basing on the nucleation and growth rate theory, Eq. (13), fails in the modeling to predict on-line crystallization at high-speed melt spinning [36], may be due to the failure of the nucleation rate approach at high stresses and supercoolings (nucleative colaps). Under such conditions, the transition mechanism changes to a virtually homogeneous transformation throughout the polymer, much more rapid then the nucleated growth. The spinline oriented crystallization kinetics at higher stresses is adequately described in the process modelling by Eq. (12) with the oriented crystallization coefficient A.

Simulation results presented by Spruiell [34] for melt spinning of iPP show that crystallization in the spinline is controlled by a balance between factors that enhance crystallization rate and the tendency for cooling of the melt to suppress crystallization. The crystallization kinetics is controlled primarily by the nature of the polymer and its molecular weight, as well as by the level of amorphous orientation developed at the spinline. The main variables affecting amorphous orientation are those affecting the tensile stress, i.e. the polymer viscosity, spinning speed and mass output [34]. In the pneumatic process, the spinning speed is controlled by the velocity of the air jet. Molecular orientation is controlled to a lesser extent by the extrusion temperature and cooling by the air. Many experimental observations of melt spinning has been rationalized for various polymers basing on the results of such simulations indicating the material and process parameters of primary or secondary importance [34].

The material parameters used in the modeling of air-drawing of iPP melt are listed in Table 1.

Table 1
The material parameters of iPP used in the modelling of pneumatic air-drawing

Parameters [units]	Value [Reference]		Parameters [units]	Value [Reference]	
ρ_0 [g/cm^3]	1.145	[18]	$T_{\max}$ [K]	338	[16]
ρ_1 [g/cm^{3}K]	9.030×10^{-4}	[18]	$K_{\max}$ [1/s]	0.55	[16]
C_{p0} [J/gK]	1.5358	[27]	$D_{1/2}$ [K]	60	[16]
C_{p1} [J/gK^2]	1.013×10^{-2}	[27]	A	500	[17]
Δh [J/g]	165	[28]	E_a/k [K]	5292	[28]

The mathematical model of the melt air-drawing, Eqs. (1)–(3), (5), (6), (11), (12), leads to five first-order differential equations for the axial profiles of the filament temperature $T(z)$, velocity $V(z)$, tensile force $F(z)$, degree of crystallinity $X(z)$, and the rheological extra-pressure $p_{rh}(z)$. Runge-Kutta numerical integration procedure has been used to compute the profiles. Boundary conditions for the numerical procedure require the initial conditions for each profile at the melt extrusion point $z = 0$. The initial conditions for four profiles are predetermined and well controlled in the process, i.e. the initial polymer temperature $T(z = 0) = T_0$, extrusion velocity of the polymer melt $V(z = 0) = 4W/[\pi D_0^2 \rho(T_0)]$ from a circular orifice of a diameter D_0, zero initial crystallinity $X(z = 0) = 0$, and zero rheological extra-pressure $p_{rh}(z = 0) = 0$.

The initial tensile force $F(z = 0)$ is adjusted to the condition $F(z = L) = 0$ at the end of the process line where the filaments are deposited onto the collector at zero tensile force at the non-woven formation.

The highest pneumatic tensile forces are exerted on the polymer discharged from the spinneret orifice located on the symmetry axis of the air jet and directed along the z-axis. Computations of the air-drawing dynamics base on the mathematical model of melt spinning [17] adopted for the pneumatic process [39]. The model applies to the range of the process z-axis where the local air velocity exceeds velocity of the polymer filament. Axial profiles $V(z)$, $T(z)$, $\Delta p(z)$ and $p_{rh}(z)$ of the pneumatic process are computed as values averaged over the filament cross-section at thin-filament approximation.

4. The results

The aim of the model computations is to study the influence of the most important process and material parameters on the dynamics of air-drawing, filament attenuation and structure of the fibers obtained in the pneumatic melt spinning of iPP melt with the use of Laval nozzle. An influence of the air compression ΔP_0^{air} at the nozzle inlet, polymer mass output W, the diameter D_0 of the melt extrusion orifice, the polymer average molecular weight M_w, and the initial melt temperature T_0 is analysed. The role of geometry of the spinneret-Laval nozzle system, as well as the spinneret-to-collector distance is also investigated.

In the example computations, ranges of the collector distance are determined at which the model predicts stationary air-drawing of the iPP melt vs. the average molecular weight M_w, the initial polymer temperature T_0 and the air compression ΔP_0^{air} at the nozzle inlet. Figures 3a,b illustrate the maximum collector distance as dependent on M_w and the extrusion temperature T_0, predicted in the computations for specified geometry of the die assembly and several air compression values. Above the maximum collector distance, the simulations predict an extremely strong increase of the local elongation rate of the melt which may lead to unlimited thinning of the filament concentrated on a very short range of the z-axis and to filament failure due to concentration of high tensile stresses.
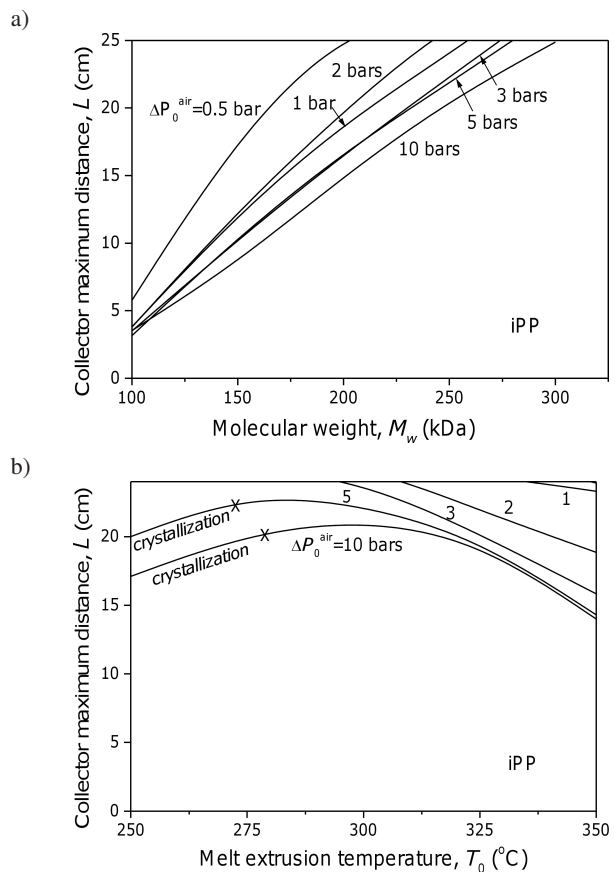

Fig. 3. Maximum collector distance vs. average molecular weight M_w of iPP at $T_0 = 300°$C (a), vs. melt extrusion temperature T_0 at $M_w = 250,000$ (b), predicted for several air compression values ΔP_0^{air}. Polymer mass output $W = 0.04$ g/s, extrusion orifice diameter $D_0 = 0.7$ mm

The simulation results indicate that thinner filaments are obtained at higher collector-to-spinneret distance. The process parameters ensuring stationary simulation of the air-drawing of the polymer at the furthest possible collector distances are selected, i.e. without breaking of the filament due to extreme increase in the elongation rate. Crystallization of iPP on the air-drawing line is predicted for higher air compressions ΔP_0^{air} in the Laval nozzle and lower melt extrusion temperatures, i.e. before achieving the collector.

Figures 4a-f illustrate axial profiles of the filament velocity, diameter, temperature, elongation rate, air drag and rheological extra-pressure obtained in the computations at the optimal collector distance $L = 20$ cm for iPP with the molecular weight $M_w = 250,000$ extruded at $T_0 = 300°$C. For the air compression $\Delta P_0^{air} = 1$ bar, the filament velocity predicted at the collector, $L = 20$ cm, (Fig. 4a) is comparable with the values obtained in the classical high-speed melt spinning processes [34, 35, 38]. Values of the filament velocity of are expressed in m/min units commonly used in the publications on fiber formation. When the air compression is increased to 2 bars, the predicted filament velocity at the collector is nearly doubled, and at the compression of 5 bars it is almost three times higher, while the final filament diameter at the collector determined from the mass balance Eq. (1) decreases (Fig. 4b).
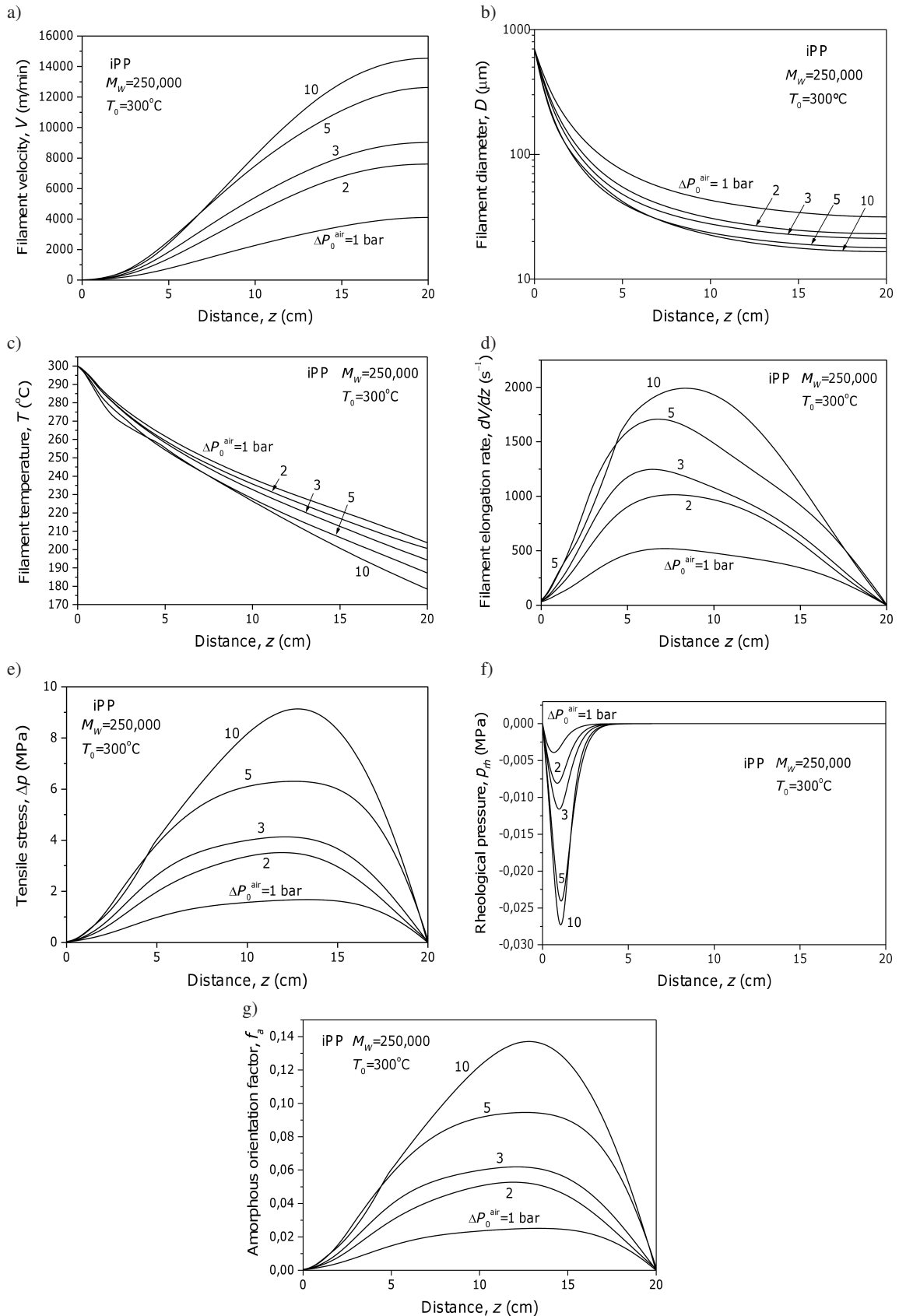
a)

b)

c)

d)

e)

f)

g)

Fig. 4. Axial profiles of iPP filament velocity (a), diameter (b), temperature (c), elongation rate (d), tensile stress (e), rheological extra-pressure (f), amorphous orientation factor (g) predicted for several values of ΔP_0^{air}. $M_w = 250,000$, $T_0 = 300°C$, $W = 0.04$ g/s, $D_0 = 0.7$ mm, $L = 20$ cm

The simulations predict significant narrowing of the filament at the initial range 2–3 cm of the air-drawing axis, mainly in the range of the Laval nozzle, as a result of the aerodynamic tensile forces concentrated at the beginning of the filament from the entire z-axis. Then, it is essential to maintain high air jet velocity on a long range of the process axis to obtain super-thin fibres. Fiber diameter predicted in the computations for the selected iPP grade at the optimum collector distance of 20 cm is 23.1, 17.8 and 16.6 μm for the air compressions 2, 5 and 10 bars, respectively. The filament diameter at a distance of 20 cm from the spinneret predicted for high-speed melt spinning of iPP is by an order of magnitude higher, much above 200 μm at M_w from the range 110,000–230,000 [34]. The filament attenuation in high-speed spinning of iPP terminates at a distance of 100–150 cm from the spinneret, at the final diameter above 30 μm. This indicates much higher elongation rates of the filament in the pneumatic process, concentrated in the initial range of the spinning axis.

The computations predict no on-line crystallization of iPP on the air-drawing axis for the melt extrusion temperature of 300°C usually applied for this polymer in the pneumatic processes. Without crystallization on the spinning axis, a monotonic decrease of the filament temperature by 100–120°C on the entire process axis is predicted (Fig. 4c). The fibres fall down onto the collector in the molten state at temperatures much exceeding the glass transition point T_g and may crystallize in the relaxed, unstressed state during cooling on the collector. The simulation results of classical high-speed melt spinning of iPP from the M_w range 110,000–230,000 and experimental measurements indicate [34] that the melt temperature drops down only by about 30°C at the distance of 20 cm from the spinneret, and the crystallization starts at a distance of about 80–100 cm depending upon M_w. This is an indication of much higher cooling rate of the melt in the pneumatic process vs. high-speed melt spinning.

In the stationary processes, the polymer elongation rate is determined by the axial gradient of the filament velocity dV/dz. At the air compression of 2 bars, the predicted elongation rate (Fig. 4d) is 5–6 times higher that in the classical high-speed spinning [35, 38]. This is a consequence of high concentration of the aerodynamic forces in the narrow range of the process axis where the polymer temperature is the highest and viscosity the lowest. When the air compression increases, the elongation rate strongly increases and reaches a maximum at 1/3 of the spinning axis. The model predicts zero elongation rate at the collector where the fibers fall freely onto it and form the nonwoven. Similar axial profiles show the tensile stress $\Delta p(z)$ and the amorphous orientation factor $f_a(z)$ predicted in the simulations, with the maximum on the axis and zero value at the collector. The maximum of $\Delta p(z)$ and $f_a(z)$ is shifted towards the collector and is positioned nearly at the midway of the spinning axis (Figs. 4e,g). In the case of $\Delta P_0^{air} = 2$ bars, the predicted maximum value of f_a is low, only 0.05. The increase of the inlet air compression to 10 bars increases f_a to 0.13. With such low values of the amorphous orientation factor of iPP, the model does not predict significant influence of oriented crystallization on the air-drawing dynamics, before deposition of the fibers on the collector. The simulation results show that contrary to high-speed melt spinning of iPP [34], the pneumatic process with free deposition of fibers onto the collector, as a nonwoven, does not produce birefringent fibers with oriented amorphous and crystalline components.

Figure 4(f) illustrates axial profiles of the negative rheological extra-pressure created in the filament. The extra-pressure is predicted in a very short range of about 2.5 cm of the spinning axis. Maximum value of the absolute extra-pressure is located in the range of the Laval nozzle narrowing, at a distance of 7–10 mm from the spinneret, and increases significantly with increasing ΔP_0^{air}. The negative extra-pressure created under the condition of uniaxial molecular orientation may cause longitudinal cavitations in the oriented melt and longitudinal burst splitting of the filament into a number of sub-filaments. Splitting of the polypropylene filament into several tens or even hundreds of microfibers was reported for the pneumatic Nanoval process under supersonic air jet [4, 5].

Spontaneous formation of longitudinal cavities was observed by the real-time high-speed video microscopy at the exit of capillary die during extrusion of linear polyethylene melt when the tensile stress at the die exceeded a critical value [40]. Experimental observations of the cavitation in polypropylene melt during tensile drawing led to the conclusion that cavitation in the amorphous phase has a homogeneous nature and is controlled by the melt cohesive forces [41].

An average diameter of the sub-filaments created during the ideal hypothetical splitting under the negative extra-pressure $p_{rh}(z_s)$ at a point z_s is estimated by the formula [23]

$$d(z_s) \cong -4\gamma(z_s)/p_{rh}(z_s), \tag{14}$$

with the assumption that the extra-pressure energy converts totally into the surface energy of created subfilaments, where $-p_{rh}(z_s) \gg 4\gamma(z_s)/D(z_s)$ and $\gamma(z_s) = \gamma_0 - \gamma_1 [T(z_s) - 296]$ is the surface tension of the iPP melt with $\gamma_0 = 2.94 \times 10^{-4}$ N/cm, $\gamma_1 = 5.60 \times 10^{-7}$ N/(cmK). The melt surface tension is controlled by the cohesive forces and depends on the temperature. Then, the melt temperature influences diameter and number of the sub-filaments.

Figure 5 presents diameter of the iPP filaments vs. the air compression ΔP_0^{air} for $M_w = 250,000$ and the melt extrusion at $T_0 = 300°C$, predicted for fibrylar splitting, as well as those without the splitting obtained at the collector distance of 20 cm. In the process without splitting, the filament diameter strongly decreases from 700 μm at the extrusion point to about 40, 31, 23 and 21 μm at the collector for the air compression of 0.5, 1, 2 and 3 bars, respectively. Increasing of the air compression above 3 bars leads to further decrease of the diameter at the collector, but the decrease is limited to about 17 μm.
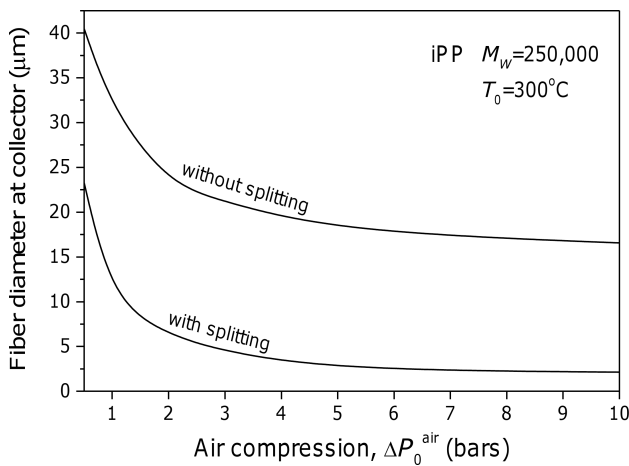
Fig. 5. Diameter of iPP filament at the collector vs. air compression ΔP_0^{air} in the process without splitting and the average sub-filament diameter in the ideal splitting predicted for $M_w = 250,000$ and $T_0 = 300°C$; mass output $W = 0.04$ g/s, orifice diameter $D_0 = 0.7$ mm, collector distance $L = 20$ cm

In the ideal splitting under the maximum absolute value of the rheological pressure, the sub-filament diameter decreases significantly with increasing the air compression, from about 23 μm to 10, 6.3 and 4.4 μm at $\Delta P_0^{air} = 0.5, 1, 2$ and 3 bars, respectively. At higher air compressions, $\Delta P_0^{air} > 3$ bars, further decrease of the sub-filament diameter is limited to about 2 μm. The number of sub-filaments with average diameter $d(z_s)$ created at the point z_s in the splitting of the filament of diameter $D(z_s)$ is given by $[D(z_s)/d(z_s)]^2$. The number of sub-filaments predicted for iPP at $M_w = 250,000$ and $T_0 = 300°C$ is about 390 for $\Delta P_0^{air} = 0.5$ bars, 670, 1720, 3090 for the air compression of 1, 2 and 3 bars, respectively.

The splitting into sub-filaments under the internal pressure in the Laval nozzle is named "the Nanoval effect", after the company which applied the pneumatic process. The experimental data [4, 5] show that continuous filaments of polypropylene with a broad diameter distribution in the range of 2–20 μm are created in the Nanoval process, with the average number of sub-filaments per single extrusion orifice being about 800 for the thinnest (2 μm) and 2 for the thickest (20 μm) ones. High number of sub-filaments per single extrusion orifice observed in the Nanoval process may result from the predicted splitting into tens or hundreds of sub-filaments under the internal pressure, while the broad diameter distribution – from a variation in the number of microfibers formed in the splitting of each filament along the spinning beam.

The plots in Fig. 5 indicate the maximum and minimum filament diameter in the distribution, predicted in the computations for the real process with a differentiated level of splitting of the filaments, between no splitting and the ideal splitting with the maximum number of sub-filaments with the diamater determined from Eq. (12). In the computations, we assume that the filaments are created with a wide range of the diameter, between 20–30 μm as predicted at the upper limit of the distribution and 2–5 μm in the lower limit. The upper and lower limits of the diamater distribution significantly decrease

with increasing air compression ΔP_0^{air} in the Laval nozzle. A significant decrease of the filament diameter in the nonwoven was observed experymantally in the Nanoval process for iPP with increasing the air compression for various processing parameters [4, 5]. However, lack of experimental data in the literature on melt spinning with the use of Laval nozzle does not allow for systematic comparison with the model predictions.

Figure 6 shows an influence of the molecular weight M_w of iPP on the upper and lower limits of the diameter distribution predicted for $\Delta P_0^{air} = 2$ bars, melt extrusion temperature $T_0 = 300°C$, mass output $W = 0.04$ g/s, orifice diameter $D_0 = 0.7$ mm, and the collector distance $L = 20$ cm. With increasing M_w, the diameter distribution widens due to the increase of the maximum diameter and the decrease of the diameter of sub-filament in the ideal splitting. This tendency is characteristic for relatively wide range of M_w between 200,000 and 300,000. With increasing molecular weight in this range, the predicted diameter of sub-filaments in the splitting decreases from about 11 μm to 5 μm, while the maximum diameter increases from about 20 μm to 30 μm. Computer simulations made by other authors [34] on classical melt spinning of iPP indicate that the process dynamics is also influenced by the molecular weight distribution characteristics M_w/M_n.
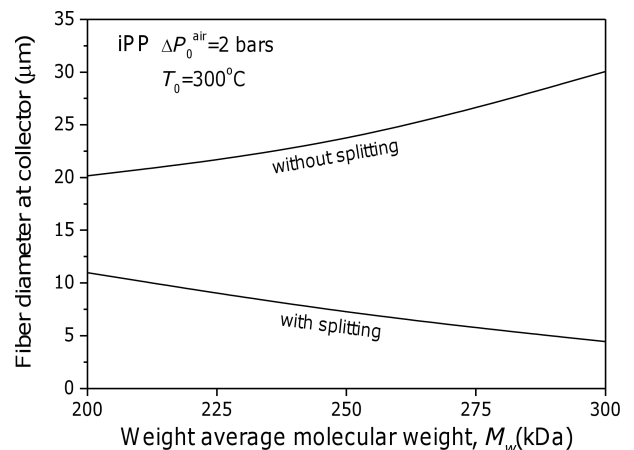

Fig. 6. Diameter of iPP filament at the collector vs. average molecular mass M_w computed for air compression $\Delta P_0^{air} = 2$ bars in the process without splitting and the diameter of sub-filament in the ideal fibrilar splitting, $T_0 = 300°C$, $W = 0.04$ g/s, $D_0 = 0.7$ mm, $L = 20$ cm

At higher polymer extrusion temperatures T_0, a decrease of the diameter of the filaments is predicted for the process without splitting, as well as for the splitting (Fig. 7) with an increase in the number of sub-filaments.

The computations indicate that to create super-thin fibres in the pneumatic process in the Laval nozzle, adequate choice of the melt extrusion temperature, average polymer molecular weight, air compression in the nozzle inlet and the collector distance is required. Polymer mass output W and the orifice diameter D_0 may have also influence the process dynamics and the fiber thickness. Influence of W and D_0 on the iPP

filaments' diamater is presented in Figs. 8 and 9. The increase of the mass output W in the range 0.02–0.16 g/s leads to a strong increase of the maximum filament diameter by a factor of 4–5 (Fig. 8), while diameter of the sub-filaments in the splitting increases in the range 2–9 μm. It is predicted that in order to obtain super-thin fibres it is beneficial to apply low mass output values. This conclusion is confirmed by the experimental research on the distribution of the diameter of iPP filaments obtained in the Nanoval process where the average filament diameter increases with increasing the polymer mass output [5, 42].
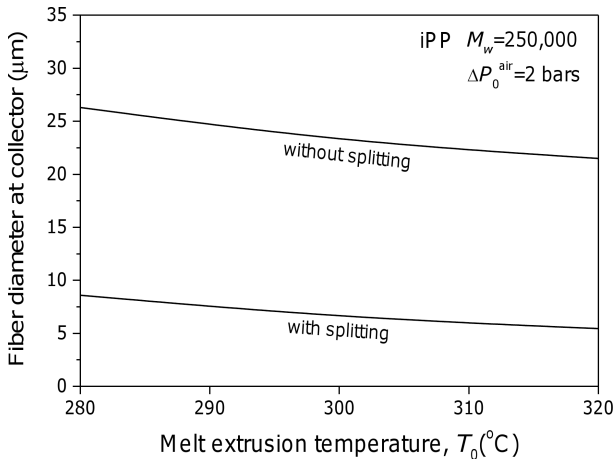

Fig. 7. Diameter of iPP filament at the collector vs. melt extrusion temperature T_0 computed for air compression $\Delta P_0^{air} = 2$ bars in the process without and with the splitting. $M_w = 250,000$; $W = 0.04$ g/s, $D_0 = 0.7$ mm, $L = 20$ cm
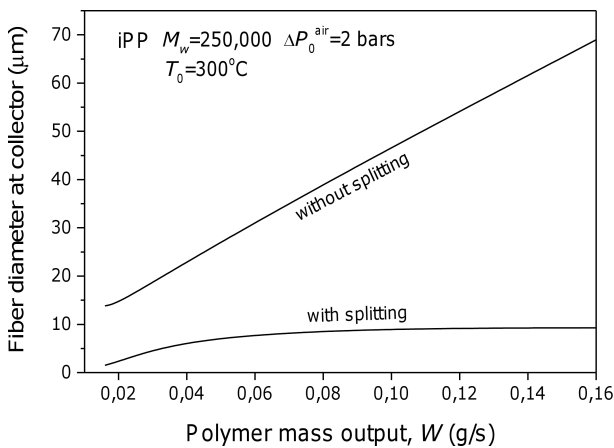

Fig. 8. Diameter of iPP filament on the collector vs. polymer mass output W computed for air compression $\Delta P_0^{air} = 2$ bars in the process without and with fibrylar splitting. $M_w = 250,000$, $D_0 = 0.7$mm, $L = 20$cm

The diameter D_0 of the melt extrusion orifice also significantly influences diameter of the fibers (Fig. 9). With increasing D_0 in the range 0.35–1.05 mm, the upper limit of the diameter distribution of iPP filaments increases in the range 21–24 μm only, while the lower limit increases much strongly in the range 0.7–18 μm. No experimental data concerning the influence of the melt extrusion orifice diameter on the pneumatic process in the Laval nozzle is available in the literature.
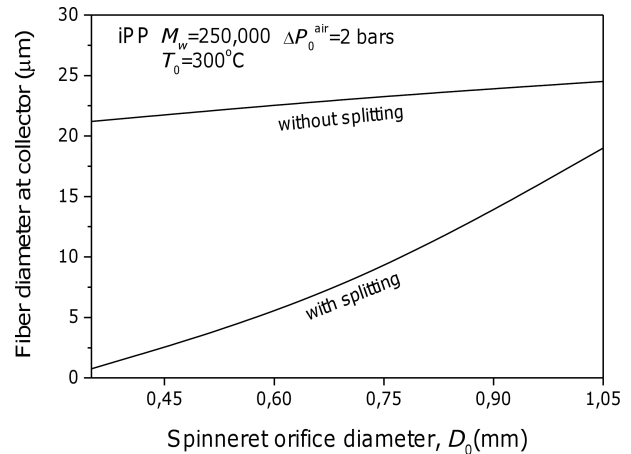

Fig. 9. Diameter of iPP filament on the collector vs. orifice diameter D_0 computed for air compression $\Delta P_0^{air} = 2$ bars in the process without and with fibrylar splitting. $M_w = 250,000$, $T_0 = 300^o$C, $W = 0.04$g/s, $L = 20$cm

5. Conclusions

The model allows to get information on the influence of a key process and material parameters on the basic air-drawing functions in pneumatic melt spinning of fibers with the use of the Laval nozzle and supersonic air jet. Significant effects taking place in fast pneumatic drawing of the polymer melt are included in the modeling.

Simulations of the aerodynamic fields in the system at the air compressions in the range of 0.5–10 bars at the inlet of the Laval nozzle predict air velocity of one Mach at the nozzle narrowing. The air velocity increases to supersonic values along the divergent exit of the nozzle for the air compressions above 1.5 bar and remains supersonic on a wide range of the computation domain outside the nozzle outlet.

For pneumatic melt spinning of fibers, the highest aerodynamic potential of the air jet locates along the jet's symmetry axis where the highest air velocity is predicted in the simulations. Directing the polymer extrusion from the spinneret orifice centrally along the air jet axis should lead to an optimal air-drawing of the polymer melt in the pneumatic melt spinning. The simulations predict a significant drop down of the air jet temperature well below 0°C which results from a rapid expansion of the air in the Laval nozzle outlet. The greater is the compression, the lower is the air jet temperature. The air pressure reduces at the nozzle outlet to the atmospheric value.

The process parameters significantly affecting the dynamics of the pneumatic melt spinning in the Laval nozzle are the air compression at the nozzle inlet, the extrusion temperature and mass output of the polymer melt, as well as the diameter of the melt extrusion orifice. The geometry of the spinneret-Laval nozzle assembly and the distance to the collector also play an important role. The main material parameter substan-

tially affecting the pneumatic process dynamics is the polymer weight average molecular weight M_w.

The air and the filament velocity profiles indicate simultaneous acceleration of both, the filament and the air, in the range of the Laval nozzle which leads to a rapid narrowing of the filament at the beginning of the process z-axis. Maintaining a high supersonic velocity of the air jet on a large range of the process axis between the spinneret and the collector, dominating a velocity of the filament, leads to aerodynamic drawing of the filament and obtaining the continuous and unentangled filaments, in contrast to melt blowing which shows a decaying air jet.

The velocity of the filament at the collector significantly increases with increasing air compression ΔP_0^{air}, from the values comparable with the classical high-speed melt spinning at the air compression of 1 bar to the values nearly twice higher at 2 bars. For larger air compressions, the take-up velocity at the collector continuosly increases and the fiber diameter at the collector decreases.

The fibers falling down onto the collector at temperatures above the polymer melting point are amorphous in the case of usually applied high extrusion temperatures of polypropylene. With no on-line crystallization along the process z-axis, isotropic crystallization of the polymer with a relaxed molecular orientation may be expected at cooling on the collector.

A negative rheological extra-pressure in the filament bulk is predicted at the beginning of the spinning axis in the Laval nozzle range, higher at higher air compressions. The negative pressure can cause melt cavitation and fibrylar splitting of the air-drawn filaments into microfibers. The diameter of the microfibers in the splitting is inversely proportional to the absolute value of the rheological extra-pressure and is controlled by the surface tension of the polymer melt.

The diameter of the fibers received on the collector and the diameter of the sub-filaments in the splitting determine upper and lower limits of the fiber diameter distribution in the nonwoven. The upper and lower limits of the diameter distribution decrease with increasing air compression in the Laval nozzle inlet, to the asymptotic limit for polypropylene of about 17 μm and 2 μm, respectively, at $M_w = 250,000$ and $T_0 = 300°C$.

With increasing the average molecular weight M_w, the diameter distribution widens due to the increase in the upper limit and decrease in the lower one. In the case of iPP, it applies to a wide range of M_w.

With increasing the melt extrusion temperature T_0, the upper and lower limits of the distribution of the fiber diameter decrease.

A strong increase of the upper limit of the fiber diameter distribution is predicted with increasing of the polymer mass output W, and a much weaker increase of the diameter limit with increasing the melt extrusion orifice diameter D_0. The lower limit of the fiber diameter distribution increases mildly with increasing W, and much more strongly with increasing D_0.

The conclusions drawn from the model computations are consistent with the very limited experimental data available in the literature on the impact of the process and material parameters on the characteristics of the fibers obtained in melt spinning of nonwovens with the use of the Laval nozzle and the supersonic air jet. It has to be emphasized that the presented simulation results provide hipothetical conclusions at several points which need to be tested experimentally.

REFERENCES

[1] R.R. Bresee and W.C. Ko, "Fiber formation during melt blowing" *Int. Nonwovens J.* 12 (2), 21–28 (2003).

[2] R.R. Bresee, "Influence of processing conditions on melt blown web structure. Part 1 – DCD", *Int. Nonwovens J.* 13 (1), 49–55 (2004).

[3] L. Jarecki and Z. Lewandowski, "Mathematical modelling of the pneumatic melt spinning of isotactic polypropylene. Part III. Computations of the process dynamics", *Fibres Textiles Eastern Eur.* 17 (1), 75–80 (2009).

[4] L. Gerking, "Method and device for the production of an essentially continous fine thread", US Pat. 6, 800, 226 B1 (2004).

[5] L. Gerking, "Nanoval process for spunbonded nowovens", *Chem. Fibers Int.* 52, 424–426 (2002).

[6] H.M. Krutka, R.I. Shambaugh, and D.V. Papavasiliou, "Effects of die geometry on the flow field of the melt blowing process", *Ind. Eng. Chem. Res.* 42, 5541–5553 (2003).

[7] T. Chen, X. Wang, and X. Huang, "Modeling the air-jet flow field of a dual slot die in the melt blowing nonwoven process", *Textile Res. J.* 74 (11), 1018–1024 (2004).

[8] H.M. Krutka, R.I. Shambaugh, and D.V. Papavasiliou, "Using computational fluid dynamics to simulate flow fields from various melt blowing dies", *Int. Nonwovens J.* 14, 2–8 (2005).

[9] A. Allimant, M.P. Planche, Y. Bailly, and L. Dembinski, "Progress in gas atomization of liquid metals by means of a De Laval nozzle", *Powder Techn.* 190, 79–83 (2009).

[10] S. Matsuo, M. Tanaka, Y. Otobe, H. Kashimura, H. Kim, and T. Setoguchi, "Effect of axisymmetric sonic nozzle geometry on characteristics of supersonic air jet", *J. Thermal Sci.* 13, 121–126 (2004).

[11] S.B. Pope, *Turbulent Flows*, Cambridge University Press, Cambridge, 2000.

[12] B.E. Launder and D.B. Spalding, *Lectures in Mathematical Models of Turbulence*, Academic Press, London, 1972.

[13] D.C. Wilcox, *Turbulence Modeling for CFD*, DCW Industries, Inc., Toronto, 1998.

[14] D.C. Wilcox, "Reassessment of the scale-determining equation for advanced turbulence models", *AIAA J.* 26, 1299–1310 (1988).

[15] D.C. Wilcox, "Multiscale models for turbulent flow", *AIAA J.* 26, 1311–1320 (1988).

[16] A. Ziabicki, *Fundamentals of Fibre Formation*, J. Wiley, London, 1976.

[17] A. Ziabicki, L. Jarecki, and A. Wasiak, "Dynamic modelling of melt spinning", *Comput. Theoret. Polymer Sci.* 8, 143–157 (1998).

[18] T. Chen and X. Huang, "Modeling polymer air drawing in the melt blowing nonwoven process", *Textile Res. J.* 73, 651–654 (2003).

[19] T. Chen, X. Wang, and X. Huang, "Effects of processing parameters on the fiber diameter of melt blown nonwoven fabrics", *Textile Res. J.* 75, 76–80 (2005).

[20] S. Kase and T. Matsuo, "Studies of melt spinning. I. On the stability of melt spinning", *J. Polymer Sci.* A-3, 2541–2554 (1965).

[21] S. Kase and T. Matsuo, "Studies on melt spinning. II. Steady-state and transient solutions of fundamental equations compared with experimental results", *J. Appl. Polymer Sci.* 11, 251–287 (1967).

[22] R.G. Larson, *Constitutive Equations for Polymer Melts and Solutions*, p. 171, Butterwoths, Boston, 1988.

[23] L. Jarecki, S. Blonski, A. Blim, and A. Zachara, "Modeling of pneumatic melt spinning processes", *J. Appl. Polymer Sci.* 125, 4402–4415 (2012).

[24] A. Ziabicki, L. Jarecki, and A. Sorrentino, "The role of flow-induced crystallization in melt spinning", *e-Polymers*, 072 (2004).

[25] J.S. Lee, D.M. Shin, H.W Jung, and J.C. Hyun, "Transient solutions of the dynamics in low-speed fiber spinning process accompanied by flow-induced crystallization", *J. Non-Newtonian Fluid Mech.* 130, 110–116 (2005).

[26] A. Ziabicki, "The mechanisms of 'neck-like' deformation in high-speed melt spinning. 2. Effects of polymer crystallization", *J. Non-Newtonian Fluid Mech.* 30, 157–168 (1988).

[27] D.W. van Krevelen, *Properties of Polymers*, pp. 86, 463, 469, Elsevier, Amsterdam, 2000.

[28] J.E. Mark, *Physical Properties of Polymers*, pp. 424, 670, AIP Press, New York, 1966.

[29] L. Jarecki, A. Ziabicki, and A. Blim, "Dynamics of hot-tube spinning from crystallizing polymer melts", *Comput. Theoret. Polymer Sci.* 10, 63–72 (2000).

[30] R.J. Samuels, *Structured Polymer Properties*, p. 58, J. Wiley, NewYork, 1974.

[31] A. Ziabicki, "Theoretical analysis of oriented and non isothermal crystallization I. Phenomenological considerations. Isothermal crystallization accompanied by simultaneous orientation or disorientation", *Colloid Polymer Sci.* 252, 207–221 (1974).

[32] A. Ziabicki, "Crystallization of polymers in variable external conditions", *Colloid Polymer Sci.* 274, 209–217 (1996).

[33] G.C. Alfonso, M.P. Verdona, and A. Wasiak, "Crystallization kinetics of oriented poly(ethylene therephthalate) from the glassy state", Polymer 19, 711–716 (1978).

[34] J.E. Spruiell, "Structure formation during melt spinning", in *Structure Formation in Polymeric Fibers*, ed. D.R. Salem, Chap. 2, Munich, Cincinnati, 2000.

[35] K. Katayama and M. Yoon, "Polymer crystallization in melt spinning: mathematical simulation", in *High-Speed Fiber Spinning*, eds. A. Ziabicki, H. Kawai, Chap. 8, Wiley, New York, 1985.

[36] R.M. Patel and J.E. Spruiell, "Crystallization kinetics during polymer processing – analysis of available approaches for process modeling", *Polymer Eng. Sci.* 31, 730–738 (1991).

[37] R.M. Patel, J.H. Bheda, and J.E. Spruiell, "Dynamics and structure development during high-speed melt spinning of Nylon 6. II. Mathematical modeling", *J. Appl. Polymer Sci.* 42, 1671–1682 (1991).

[38] A. Ziabicki, L. Jarecki, "The theory of molecular orientation and oriented crystallization in high-speed spinning", in *High-Speed Fiber Spinning*, eds. A. Ziabicki, H. Kawai, Chap. 9, Wiley, New York, 1985.

[39] L. Jarecki, A. Ziabicki, Z. Lewandowski, and A. Blim, "Dynamics of air drawing in the melt blowing of nonwovens from isotactic polypropylene by computer modeling", *J. Appl. Polymer Sci.* 119, 53–65 (2011).

[40] Y. Son, K.B. Migler, "Cavitation of polyethylene during extrusion processing instabilities", *J. Polymer Sci. B, Polymer Phys.* 40, 2791–2799 (2002).

[41] A. Rozanski, A. Galeski, and M. Debowska, "Initiation of cavitation of polypropylene during tensile drawing", *Macromolecules* 44, 20–28 (2011).

[42] L. Gerking and M. Stobik, "Nanoval splitspinning – from coarse to nano", *Chem. Fibers Int.* 57, 210–211 (2007).